Supplementary Material: Traction Force Microscopy in Physics and Biology

Robert W. Style,[1] Rostislav Boltyanskiy,[1] Guy K. German,[1,2] Callen Hyland,[1] Christopher W. MacMinn,[1,3] Aaron F. Mertz,[1,4] Larry A. Wilen,[1] Ye Xu,[5] and Eric R. Dufresne[1,*]

[1] *Yale University, New Haven, CT 06511, USA*
[2] *Department of Bioengineering, Binghamton University, P.O. Box 6000, Binghamton, NY 13902, USA*
[3] *Department of Engineering Science, University of Oxford, Oxford 0X1 3PJ, UK*
[4] *Laboratory of Mammalian Cell Biology and Development, The Rockefeller University, 1230 York Ave, Box 300, New York, NY 10065, USA*
[5] *University of Pennsylvania, Philadelphia, PA 19104, USA*

(Dated: April 3, 2014)

I. SILICONE SUBSTRATE FABRICATION

Preparation of a silicone TFM substrate typically consists of bead deposition on a glass slide, deposition of a uniform layer of silicone, fluorescent bead deposition on the silicone surface, and finally deposition of an optional very thin layer of silicone (the thinner, the more accurate the TFM).

We create uniform layers of silicone by spin-coating the curing polymer on a glass slide. Silicone is typically prepared by mixing a curer and base. For example, a 3 kPa gel is produced by a 1:1 weight ratio mixture of CY52-276A and CY52-276B (Dow Corning Toray). Published results indicate that Sylgard 184 can be produced with Young's moduli covering nearly four orders of magnitude depending on the ratio of cure to base, [1–7]. However, we acheived reliable TFM with Sylgard only for moduli above about 50 kPa. After mixing, the silicone should be degassed in a vacuum chamber until there are no visible air bubbles. In our chamber, this takes ∼1 minute for CY52-276 and ∼30 minutes for Sylgard 184. The thickness of a spin-coated film depends on spin time, speed and fluid viscosity. Once the base and cure are mixed, the silicone viscosity will change over time. Thus for reproducible results it is helpful to have a standard delay between mixing and spin-coating. When mixing, degassing and spin-coating proceed with minimal delay, a roughly 30 micron film can be created by spinning at 1000-1500 rpm for 60 sec and a 3 micron film can be created by spinning at 10000 rpm for 60 sec for both CY52 and Sylgard 184.

Fluorescent beads need to be well-spaced on the substrate surface to ensure accurate tracking of surface displacements. We deposit the beads on substrates from suspension, which allows bead spacing to be controlled by their volume fraction in suspension, and the substrate immersion time. Example images of good bead densities are shown in the supplementary example code package. In some cases, beads will attach rigidly to the substrate on their own, especially for very soft silicones. Otherwise, the beads can be covalently attached to a silanized substrate. Before deposition, the glass or silicone substrate is amine-functionalised by a minimal vapour-deposition of 3-aminopropyl triethoxysilane (Polysciences). Excess silane can compromise substrate mechanical properties. To attach beads to the amine-functionalised surface, we use carboxylate-modified fluorescent microspheres (beads) suspended in a solution containing 3.8mg/mL sodium tetraborate, 5mg/mL boric acid and 0.1mg/mL 1-ethyl-3-(3-dimethylaminopropyl)carbodiimide (EDC) (Sigma-Aldrich). For imaging at 100× and 40×, we submerge silanated substrates in suspensions of 40nm and 100nm fluorescent beads at a volume fractions of $\phi \approx 5 \times 10^{-6}$ for 60 and 240 sec, respectively.

II. SUBSTRATE CHARACTERISATION

It is important to characterise the material properties of the substrate for quantifying stresses using TFM. If the substrate stiffness $E \gtrsim 100$kPa, such as for silicone elastomers with higher cross-linking density, this can be done with a tensile test on a thin rod of the substrate material. For small deformations, the stress/strain relationship should be linear with a slope given by Young's modulus. The strain where the linear relationship breaks down should be recorded – this represents the maximum strain that should be imposed on the substrate during the TFM measurement. Poisson's ratio depends on the change in length, L, and diameter, d: for small extensions, $\nu = -(\Delta d/d)/(\Delta L/L)$. For most materials used in TFM, this value will be near 0.5. This tensile test can be quickly and crudely done by hanging weights from one end of a rod and measuring its change in length and diameter. Precise material characterisation can be achieved with commercial tensile testing equipment (e.g. Instron) [8].

Tensile testing works well for stiff materials that can support their own weight, like elastomers. However it is typically impractical for softer materials like gels, where we need to characterise mechanical properties in shear with a rheometer. A traditional rheometer works by sandwiching a slab of gel between two plates, applying a torque and quantifying the torque/deformation relationship [9]. Often one of the plates is actually a shallow

* eric.dufresne@yale.edu

cone, so that the shear strain is uniform throughout the slab. Since the instrument is constrained to work in a fixed geometry, the gel is set in the rheometer with careful temperature and humidity control (for a hydrogel). To monitor gel setting, we apply a steady oscillatory strain (frequency ~ 1 rad/sec and strain $\sim 1\%$) while recording the resulting stress over time. This *time sweep* allows us to calculate the storage modulus (related to stiffness, labeled G') and loss modulus (related to viscosity, labeled G'') as a function of time. In Fig. 1 (a), we show example data for CY-52-276 silicone gel at room temperature. Eventually G' should reach a plateau indicating that the gel is set. In this example, this occurs about two hours after mixing. Note that the modulus continues to increase slowly after two hours.

We need the cured substrate to behave like an elastic solid under static loadings. This can be checked by a frequency sweep, where G' and G'" are measured over a wide range of frequencies by applying a fixed-amplitude (strain $\sim 1\%$) oscillatory torque. The material is elastic under static loadings if G' reaches a plateau value as frequency approaches 0 rad/s with $G' \gg G''$. As TFM applications are static or involve slow loading, one should use the low frequency value of G' for characterising substrate stiffness. Fig. 1(b) on silicone gel shows a non-zero zero-frequency storage modulus showing elastic behaviour for static loadings. The plot also shows how G' and G'' curves can crossover at higher frequencies. TFM analysis will only provide meaningful results when the stresses applied to the substrate are applied at much lower frequencies.

The cured substrate needs to behave linear-elastically under experimental strains so that we can use Hooke's law. We check this by performing a strain sweep, applying oscillatory strain at a constant frequency ($\sim$ 1 rad/sec) and measuring the material response over a range of strains. A linear-elastic regime is shown by plateau in G' at low strains. G' may rise at higher strains, followed by a sharp decrease, indicating strain stiffening followed by breakage. Fig. 1(c) shows linear-elastic behaviour in shear for $\lesssim 100\%$ strain in our silicone gel.

To calculate Young's modulus from G', we need the substrate's Poisson ratio. This can be measured using tensile testing in a rheometer. The gel is cured in between the plates of an rheometer, and then stresses are measured as the plates are pulled apart or compressed. The loading is *p*lane strain because the rheometer plates confine the gel so that there are no displacements in the in-plane directions, unlike in the tensile rod test. Note that stresses build up rapidly in this geometry, so the range of achievable strains is typically small. In the linear-elastic regime, extensional stress and strain are related by

$$\sigma = \frac{E(1-\nu)}{(1+\nu)(1-2\nu)}\epsilon = \frac{2G'(1-\nu)}{(1-2\nu)}\epsilon, \qquad (1)$$

where we have used the relationship $G' = \frac{E}{2(1+\nu)}$ in the second equality [10, 11]. We insert the measured value of G', and use the measured linear relationship between σ and ϵ to solve for Poisson's ratio. Fig. 1(d) shows results for tensile testing on silicone gel. With this data, and with G' from Fig. 1c, we find that $\nu = 0.495$. In general, incompressible materials like silicone or PAA gels have $\nu \approx 1/2$, and so $E \approx 3G'$.

III. DATA ANALYSIS

Having imaged the sample, we have to extract the traction stresses. This involves: (i) calculating bead positions from image data, (ii) correcting for index of refraction mismatches, (iii) correcting for drift and calculating displacements, (iv) preparing the data for Fourier transforming, and (v) using theory to calculate traction stresses.

A. Converting images to bead positions

We need to track the motion of the embedded fluorescent particles from images such as those in the Supporting Information stress calculation example. Two common techniques for converting images to bead positions are particle tracking and correlation tracking.

Particle tracking follows individual beads between images. In each image, we identify individual beads as bright, isolated spots, and find their positions by finding the centroid of each spot. We then track beads from frame to frame using particle-tracking software which assumes a maximum distance of travel between frames [12].

Particle-tracking software can also be used to find the z-position of beads from confocal image stacks: We calculate bead x-/y-positions and intensity for each image in the stack. We then use particle tracking to follow individual beads through the stack. For each bead, we plot the intensity as a function of z, and fit a Gaussian curve through the results. The peak of the Gaussian corresponds to the bead's z-position.

Particle tracking fails when particles displacements exceed the mean inter-particle spacing, as it is no longer possible to uniquely identify particle trajectories. This sets a limit on the spatial resolution that can be achieved. For time series, this problem can be avoided by increasing image frequency to avoid large displacements between images.

Correlation tracking, also known as digital image correlation [13] or particle image velocimetry [14], involves tracking constellations of particles rather than individual particles. Unlike particle tracking, correlation tracking works with the raw image pixel data; individual beads are not tracked. It compares 'before' and 'after' images to find image portions that are most similar – most highly correlated. The displacements between the images then correspond to surface displacements of the substrate. Many different implementations of correlation tracking exist, each with its own advantages and disadvantages [15].

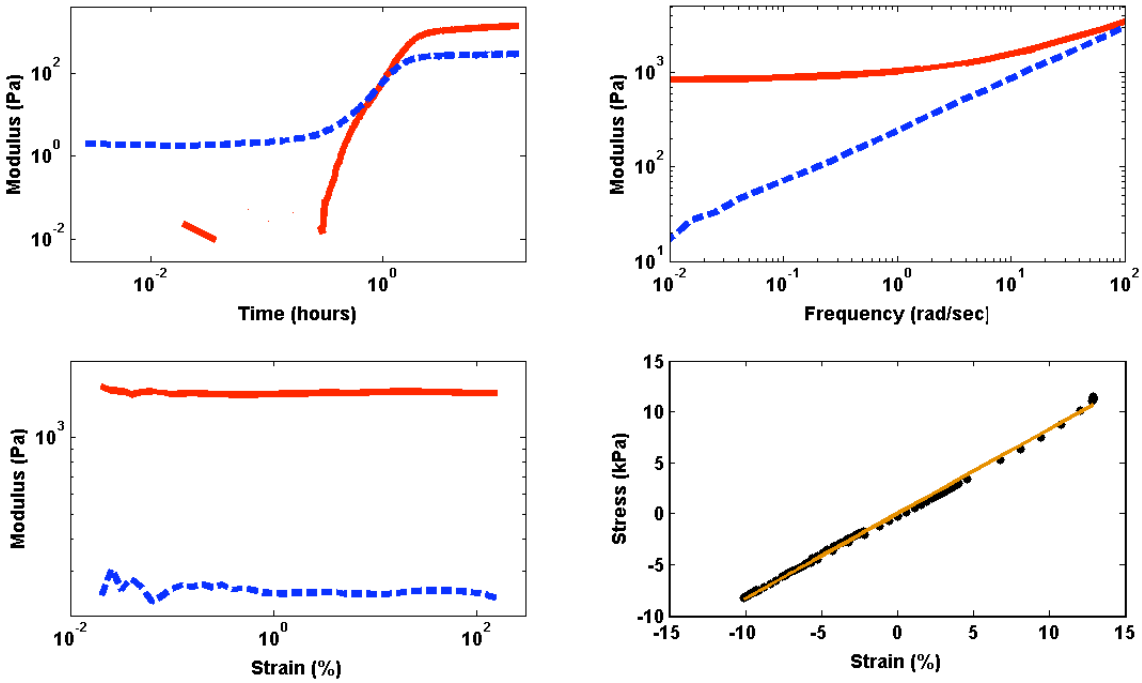

FIG. 1. Silicone rheology tests performed on rheometer ARES-LS1. G' plotted in red, solid line. G'' plotted in blue, dashed line. Plain strain data in dots, black with linear fit solid orange. (a) Time sweep at room temperature at 0.5% strain, 1 rad/sec (Top left). (b) Frequency sweep at room temperature at 0.5% strain (Top right). (c) Strain sweep at room temperature at 1 rad/sec (Bottom left). (d) Plane strain test at room temperature (Bottom right).

Particle tracking and correlation tracking can be combined to give a more powerful technique, without the individual disadvantages of the techniques. Hybrid tracking techniques are useful in scenarios where high-resolution spatial displacements are required, but particle movement between frames is too large to use particle tracking. Then we can use correlation tracking to give a rough estimate of substrate displacements, followed by particle tracking to fine tune the measurement of displacement [16].

B. Correcting for index of refraction mismatches.

Measured bead z-positions need to be corrected to account for refraction when using substrates containing layers of different materials with different refractive indices, n. Such discontinuities will often occur in TFM substrates consisting of a coating on a glass slide. They can also occur when using an immersion fluid for imaging that has a different n to the substrate. One approach for obtaining correct z-positions is to use a calibration device [17]. Alternatively, if the substrate is made of top and bottom layers with refractive indices n_t and n_b respectively, the actual z-positions of beads are related to measured positions z^* by $z \approx z^*(n_b/n_t)$ [18]. This correction is an approximation derived from ray optics, and works for objectives with Numerical Aperture (NA) $\lesssim 1.3$. For higher NA a more detailed calculation is required [18]. Glass cover slips typically have a refractive index of $n \sim 1.52$. Polyacrylamide refractive indices vary in the range $1.34 - 1.4$. The refractive index of silicone is $\sim$1.4.

C. Calculating displacements and subtracting drift

We now calculate the bead displacements induced by sample tractions for the top layer of beads. If there is no drift, the displacements are simply the difference in bead positions between the attached-sample and reference states. However typically the substrate drifts slightly on the microscope between images, and this corrupts the displacement data. We calculate the motion of the beads held rigid at the base of the substrate, which only move due to whole-sample rotation and translation. Drift-free displacements are then determined by subtracting the calculated drift rotation and translation from the measured top-bead displacements.

Without a bottom layer of beads, drift can be estimated in two ways. Firstly, we can find a section of top-layer beads that are far from any surface tractions (at least a few times the depth of the substrate). Assuming these beads are not affected by traction stresses, we

can use them as a non-moving reference to subtract drift. Secondly, we can measure the average rotation and translation of all the top-layer beads and assume that this is the sample drift. These approaches should be avoided where possible, as they only provide estimates of drift; significant errors in drift calculation can cause large errors in calculated tractions.

D. Preparing the displacement field

We now need to know the displacements on a regular grid at $z = z_0$ in the substrate for Fourier transforming later. However, the raw displacement data is randomly-scattered in the substrate at the fluorescent bead positions. We transform the data by first removing bad displacement data arising from tracking errors. Second, we interpolate the displacements to a regular grid. Third, we pad the data, and apply filters in preparation for Fourier transformation.

1. Removing bad vectors.

Tracking algorithm errors occur when a bead is paired with a different bead in subsequent frames. These tracking errors appear as abrupt discontinuities in the displacement field. If these are not removed before Fourier transforming, they cause artifacts in the calculated stress field.

We use both manual and automated techniques for removing tracking errors. In the manual technique, the bead displacements are all plotted as arrows. Viewed like this, tracking errors are typically obvious. These are selected and deleted by the user. In the automatic technique, every displacement vector is compared to an interpolated value based on other bead displacements in its neighbourhood. If the vector differs from the interpolated value by more than a threshold amount, it is discarded. This method requires specification of the size of the bead neighbourhood, the interpolation method, and the allowed tolerance between actual and interpolated values. These should be tuned for each experiment for optimal results.

2. Interpolating to a regular grid.

We next interpolate the displacement data on to a regular, 2-d grid at $z = z_0$. The interpolated data should cover the same area, and have approximately the same number of data points as the original data. For example, if there are 900 tracked beads, we choose a 29x29 grid and interpolate at each of the 30x30 nodes of the grid.

`MATLAB` has built-in options for interpolating scattered data onto a grid, such as `GRIDDATA`. For every grid point, `GRIDDATA` fits a function to a set of nearest neighbour points then evaluates the function at that grid point. `GRIDDATA` has several options that can be tuned to optimise the final stress calculation. However, one flaw with methods like this is it ensures that the fitted surface passes through all data points. This can add significant artifacts due to noise in particle location measurements. An alternative is to interpolate data at grid points by fitting a quadratic function to a user-specified number of nearest neighbour points. This smooths the data and reduces abrupt transition between values.

3. Padding the boundaries.

In situations where the force-generating structure extends outside the field of view or is close to its edge, the displacements will be non-zero at the edge of the field of view. This causes 'ringing' errors in the calculated stress field. We eliminate this artefact by padding the data – adding data points around the original data set which blend into the original data and then decay away smoothly to zero in the far field. Selection of a padding method is a delicate art and depends on the nature of the data set. In some cases, we pad our data by copying the unpadded data at the grid edges outwards to fill in the padding region, and then applying a 2-dimensional Hann window [19]. We usually choose to double the dimensions of the original data by padding.

4. Low-Pass Filter.

As described in the main text, we need to remove high-frequency noise in order to avoid stress artifacts. Thus, after padding, we use an exponential low-pass filter [20]. The cut-off wavelength should be adjusted for optimal results. When it is too small, ringing or rippling occurs in the stress field due to noise amplification. When it is too long, the fine features of the stress field will become obscured.

E. Converting displacements into stresses

We calculate the stress field from the cleaned displacement data. We Fourier transform the displacement data $\mathbf{u}(x, y, h)$ to get $\hat{\mathbf{u}}(k_x, k_y, h)$ evaluated on a regular grid of wavenumbers (k_x, k_y). We calculate $Q_{ij}(k_x, k_y, h)$ for each pair of wavenumbers, and then use Equation (2) below to convert $\hat{\mathbf{u}}$ into the Fourier-transformed stresses $\hat{\sigma}(k_x, k_y, h)$. Finally we inverse Fourier transform $\hat{\sigma}$ to obtain the traction stresses σ. Note that here we assume that the top layer of beads are at the surface, so $z_0 \approx h$. Using an experimental setup where $z_0 \neq h$ is not recommended, as it compromises short wavelength resolution. However tractions can still be extracted, using a modified Q [4].

F. The Q matrix

In §3, we showed that displacements and stresses are linearly related in Fourier space, with

$$\hat{\sigma}_{iz}(k_x, k_y, z = h) = Q_{ij}(k_x, k_y; h)\, \hat{u}_j(k_x, k_y, z = h), \quad (2)$$

with summation over repeated indices. The matrix $\boldsymbol{Q}$ is [4]

$$\boldsymbol{Q} = \frac{E}{2(1+\nu)} \left\{ \begin{bmatrix} 0 & 0 & ik_x \\ 0 & 0 & ik_y \\ \left(\frac{2\nu}{1-2\nu}\right) ik_x & \left(\frac{2\nu}{1-2\nu}\right) ik_y & 0 \end{bmatrix} \right. \quad (3)$$

$$\left. + \begin{bmatrix} 1 & 0 & 0 \\ 0 & 1 & 0 \\ 0 & 0 & \frac{2-2\nu}{1-2\nu}, \end{bmatrix} \frac{\partial \boldsymbol{M}}{\partial h}\, \boldsymbol{M}^{-1} \right\},$$

where $\boldsymbol{M} = \boldsymbol{S}\sinh(kh) + \boldsymbol{C}h\cosh(kh)$ and

$$\boldsymbol{S} = \begin{bmatrix} (3-4\nu)k_x^2 + 4(1-\nu)k_y^2 & -k_x k_y & -ihk_x \\ -k_x k_y & 4(1-\nu)k_x^2 + (3-4\nu)k_y^2 & -ihk_y \\ -ik^2 h k_x & -ik^2 h k_y & (3-4\nu) \end{bmatrix} \quad (4)$$

and

$$\boldsymbol{C} = \begin{bmatrix} kk_x^2 & kk_x k_y & 0 \\ kk_x k_y & kk_y^2 & 0 \\ 0 & 0 & -k \end{bmatrix} \quad (5)$$

with $k = \sqrt{k_x^2 + k_y^2}$. For the special case of $k = 0$,

$$\boldsymbol{Q}(k_x = k_y = 0; h) = \frac{E}{2h(1+\nu)} \begin{bmatrix} 1 & 0 & 0 \\ 0 & 1 & 0 \\ 0 & 0 & \frac{2-2\nu}{1-2\nu} \end{bmatrix}. \quad (6)$$

When out-of-plane stresses are negligible, $\sigma_{zz}(z = h) \equiv 0$, and the solution simplifies significantly [21, 22]. Then,

$$\hat{\sigma}_{xz} = \frac{Ek_x}{2(1-\nu^2)k} \frac{(3-4\nu)\cosh^2(kh) + (1-2\nu)^2 + (kh)^2}{(3-4\nu)\sinh(kh)\cosh(kh) + kh} (k_x\hat{u}_x - k_y\hat{u}_y) - \frac{Ek_y \cosh(kh)}{2(1+\nu)k\sinh(kh)} (k_x\hat{u}_y - k_y\hat{u}_x), \quad (7)$$

$$\hat{\sigma}_{yz} = \frac{Ek_y}{2(1-\nu^2)k} \frac{(3-4\nu)\cosh^2(kh) + (1-2\nu)^2 + (kh)^2}{(3-4\nu)\sinh(kh)\cosh(kh) + kh} (k_x\hat{u}_x + k_y\hat{u}_y) + \frac{Ek_x \cosh(kh)}{2(1+\nu)k\sinh(kh)} (k_x\hat{u}_y - k_y\hat{u}_x). \quad (8)$$

IV. EXAMPLE CODE

Along with this Supporting Information, we have provided a package with example `MATLAB` code showing how to calculate traction stresses. The package contains data for an Aplysia Californica bag-cell-neuron growth cone on a soft, silicone TFM substrate. It includes an image of the cell, and two fluorescent images of the surface beads with the cell in place, and after its removal.

The code takes measured bead positions from the two fluorescent images, and converts them into traction stresses and strain energy density [23]. The example provided is for 2d traction stresses – the growth cone is assumed to only exert in-plane forces on the substrate. This is typically a good assumption for cells (e.g. [21, 22]), and allows traction stresses to be calculated from measurements of in-plane displacements of the fluorescent beads. The code can be straightforwardly modified to calculate 3d traction stresses.

The code package contains three `.tif` files (images), two `.mat` files (displacement data, and cell outline data), and six `.m` files. Run `master.m` to convert displacement data into traction forces, and display the results.

[1] D. Armani, C. Liu, and N. Aluru, in *Proceedings of the IEEE Micro Electro Mechanical Systems (MEMS)* (1999) pp. 222–227.

[2] L. Chen, G. K. Auernhammer, and E. Bonaccurso, Soft Matter **7**, 9084 (2011).

[3] R. Merkel, N. Kirchgeßner, C. M. Cesa, and B. Hoffmann, Biophys. J. **93**, 3314 (2007).

[4] Y. Xu, W. C. Engl, E. R. Jerison, K. J. Wallenstein, C. Hyland, L. A. Wilen, and E. R. Dufresne, Proc. Natl. Acad. Sci. U.S.A. **107**, 14964 (2010).

[5] D. Fuard, T. Tzvetkova-Chevolleau, S. Decossas, P. Tracqui, and P. Schiavone, Microelectron. Eng. **85**, 1289 (2008).

[6] C. M. Cesa, N. Kirchgeßner, D. Mayer, U. S. Schwarz, B. Hoffmann, and R. Merkel, Rev. Sci. Instrum. **78**, 034301 (2007).

[7] M. Ochsner, M. R. Dusseiller, H. M. Grandin, S. Luna-Morris, M. Textor, V. Vogel, and M. L. Smith, Lab Chip **7**, 1074 (2007).

[8] H. Kuhn and D. Medlin, *Object Oriented Perl: ASM Handbook Volume 08: Mechanical Testing and Evaluation* (ASM International, USA, 2000).

[9] R. Larson, *Object Oriented Perl: A Structure and Rheology of Complex Fluids* (Oxford University Press, USA, 1998).

[10] L. D. Landau and E. M. Lifshitz, *Course of Theoretical Physics, Volume 7: Theory of Elasticity, Third Edition* (Pergamon Press, 1986).

[11] T. M. Atanackovic and A. Guran, *Theory of Elasticity for Scientists and Engineers* (Birkhauser, 2000).

[12] D. L. Blair and E. R. Dufresne, "The matlab particle tracking code repository," Http://physics.georgetown.edu/matlab/.

[13] T. Chu, W. Ranson, and M. Sutton, Exp. Mech. **25**, 232 (1985).

[14] C. Willert and M. Gharib, Exp. Fluids **10**, 181 (1991).

[15] M. Raffel, C. E. Willert, and J. Kompenhans, *Particle Image Velocimetry: A Practical Guide; with 24 Tables* (Springer, 1998).

[16] E. A. Cowen, S. G. Monismith, E. A. Cowen, and S. G. Monismith, Exp. Fluids **22**, 199 (1997).

[17] K. Jensen, D. Weitz, and F. Spaepen, Rev. Sci. Instrum. **84**, 016108 (2013).

[18] E. Hecht, *Optics, Fourth Edition* (Addison-Wesley, 2001).

[19] B. A. Shenoi, *Introduction to digital signal processing and filter design* (John Wiley & Sons, 2005).

[20] S. T. Bow, *Pattern recognition and image preprocessing* (CRC Press, 2002).

[21] J. C. del Álamo, R. Meili, B. Alonso-Latorre, J. Rodríguez-Rodríguez, A. Aliseda, R. A. Firtel, and J. C. Lasheras, Proc. Natl. Acad. Sci. U.S.A. **104**, 13343 (2007).

[22] X. Trepat, M. R. Wasserman, T. E. Angelini, E. Millet, D. A. Weitz, J. P. Butler, and J. J. Fredberg, Nat. Phys. **5**, 426 (2009).

[23] A. F. Mertz, S. Banerjee, Y. Che, G. K. German, Y. Xu, C. Hyland, M. C. Marchetti, V. Horsley, and E. R. Dufresne, Phys. Rev. Lett. **108**, 198101 (2012).